# Characterizing Multisubevent Earthquakes Using the Brune Source Model

Meichen Liu\*1<sup>10</sup>, Yihe Huang<sup>10</sup>, and Jeroen Ritsema<sup>1</sup>

#### **ABSTRACT**

Although the Brune source model describes earthquake moment release as a single pulse, it is widely used in studies of complex earthquakes with multiple episodes of high moment release (i.e., multiple subevents). In this study, we investigate how corner frequency estimates of earthquakes with multiple subevents are biased if they are based on the Brune source model. By assuming complex sources as a sum of multiple Brune sources, we analyze 1640 source time functions of  $M_{\rm w}$  5.5–8.0 earthquakes in the seismic source characteristic retrieved from deconvolving teleseismic body waves catalog to estimate the corner frequencies, onset times, and seismic moments of subevents. We identify more subevents for strike-slip earthquakes than dip-slip earthquakes, and the number of resolvable subevents increases with magnitude. We find that earthquake corner frequency correlates best with the corner frequency of the subevent with the highest moment release (i.e., the largest subsevent). This suggests that, when the Brune model is used, the estimated corner frequency and, therefore, the stress drop of a complex earthquake is determined primarily by the largest subevent rather than the total rupture area. Our results imply that, in addition to the simplified assumption of a radial rupture area with a constant rupture velocity, the stress variation of asperities, rather than the average stress change of the whole fault, contributes to the large variance of stress-drop estimates.

#### **KEY POINTS**

- Global source time functions are investigated for the Brune source parameters of multisubevent earthquakes.
- We find that the master event corner frequencies correlate better with those of the large subevent.
- The Brune stress drop is better correlated to the stress change of the asperity with the largest moment.

**Supplemental Material** 

# **INTRODUCTION**

The classical earthquake source model proposed by J. Brune more than five decades ago (Brune, 1970) is still broadly used to understand the propagation of a fault rupture and the radiation of seismic energy. In the Brune model, a circular crack instantaneously experiences a shear dislocation due to a constant stress drop (i.e., the change of stress) on the fault. The Brune model links three key elements of an earthquake: the seismic moment, corner frequency, and stress drop with simple functions in which the seismic moment and corner frequency are the two free parameters. The Brune model predicts that the source spectrum is constant at frequencies lower than the corner frequency, and decays proportional to the square of frequency at frequencies higher than the corner frequency, an important feature for the calculation of high-frequency ground

motions for engineering applications (Papageorgiou and Aki, 1983; Purvance and Anderson, 2003; Sotiriadis et al., 2021). Numerous studies of small and large, shallow and deep, and tectonic and induced earthquakes using regional and teleseismic data are based on the Brune source model when estimating stress drops (e.g., Abercrombie, 1995; García et al., 2004; Allmann and Shearer, 2009; Baltay et al., 2011; Oth, 2013; Chen and Shearer, 2011; Huang et al., 2016; Prieto et al., 2017; Ruhl et al., 2017; Trugman et al., 2017; Wu et al., 2018; Shearer et al., 2019; Liu et al., 2020; Yu et al., 2020).

Nevertheless, it is well recognized that earthquakes are complex on a wide variety of spatial and temporal scales. The barrier (Das and Aki, 1977) and asperity (Lay and Kanamori, 1981; Lay et al., 1982) models describe stress and frictional differences on the fault plane. The rupture velocity and the moment rate during rupture expansion can change due to dynamic waves in fault damage zones (e.g., Huang and Ampuero, 2011) as well as fault curvature and segmentation

**Cite this article as** Liu, M., Y. Huang, and J. Ritsema (2023). Characterizing Multisubevent Earthquakes Using the Brune Source Model, *Bull. Seismol. Soc. Am.* **113**, 577–591, doi: 10.1785/0120220192

© Seismological Society of America

<sup>1.</sup> Department of Earth and Environmental Sciences, University of Michigan, Ann Arbor, Michigan, U.S.A., https://orcid.org/0000-0001-7952-340X (ML); https://orcid.org/0000-0001-5270-9378 (YH)

<sup>\*</sup>Corresponding author: meichenl@umich.edu

(e.g., Ando and Kaneko, 2018; Ulrich et al., 2019). The complexity of rupture processes is not only evident for  $M_{\rm w} > 7$ earthquakes (e.g., Ye et al., 2016; Hayes, 2017), but also for smaller earthquakes (e.g., Boatwright, 1984). Using local seismic arrays, moment rate fluctuations have been observed for  $M_{\rm w}$  < 3.5 earthquakes in the Charlevoix, Quebec, seismic zone (Li et al., 1995; Fischer, 2005), on the San Andreas fault (Abercrombie, 2014; Wang et al., 2014; Abercrombie et al., 2020), and in the 2008 Mogul, Nevada, swarm (Ruhl et al., 2017). Danré et al. (2019) used the Gaussian source model to systematically analyze the source complexity for seismic source characteristic retrieved from deconvolving teleseismic body waves (SCARDEC) source time function (STFs; Vallée and Douet, 2016). They observed increasing source complexity with earthquake magnitude and an important scaling of the moment of subevent with the earthquake moment by a factor of 0.8. For the Brune source model, the source complexity may cause earthquake source spectra to deviate from the frequency-squared spectral decay for moderate to large (e.g., Luco, 1985; Atkinson, 1993; Beresnev and Atkinson, 2001; Denolle and Shearer, 2016; Yin et al., 2021) and small earthquakes (e.g., Uchide and Imanishi, 2016). The Brune source model has also been modified to include two corner frequencies to explain the deviation (Archuleta and Ji, 2016; Denolle and Shearer, 2016; Uchide and Imanishi, 2016; Ji and Archuleta, 2021).

For many earthquakes, however, there are insufficient data to model source complexity. It is also not a common practice to use complex source models to predict earthquake ground motions. Therefore, the Brune source model is still frequently used to estimate source parameters and ground motions regardless of earthquake source complexity. This poses a fundamental question: What is measured by the Brune source model when it is applied to complex earthquakes?

Here, we investigate what kind of source properties are represented by the Brune source model for earthquakes with multiple episodes of high moment release (i.e., multiple subevents). We first quantify earthquake source complexity by analyzing the number and source properties of subevents in STFs of hundreds of  $M_{\rm w}$  5.5–8.0 earthquakes in the SCARDEC catalog (Vallée and Douet, 2016). We describe and decompose the STF as a sum of Brune sources, and estimate corner frequencies and seismic moments of subevents. By comparing measured source complexity to that observed by Danré et al. (2019), we further understand the scaling relationship between the source complexity and the subevent moment. We also derive the theoretical source spectrum of a complex earthquake with two Brune subevents. Using both SCARDEC analysis and theoretical derivation, we compare the earthquake's overall corner frequency to the corner frequencies of individual subevents and show how earthquake corner frequency and stress drop depend on the temporal spacing and relative moments of subevents.

#### STF DECOMPOSITION

In the time domain, the Brune source is defined as

$$\Omega(t, t_0, f_c, M_0) = M_0 (2\pi f_c)^2 (t - t_0) e^{-2\pi f_c (t - t_0)} H(t - t_0), \quad (1)$$

in which  $H(t-t_0)$  is the Heaviside function,  $t_0$  is the onset time of the rupture,  $M_0$  is the seismic moment, and  $f_c$  is the corner frequency that is scaled to a characteristic rupture time  $1/f_c$ . The Brune model predicts a far-field spectrum:

$$\Omega(f f_c, M_0) = \frac{M_0}{1 + \frac{f^2}{f_c^2}},\tag{2}$$

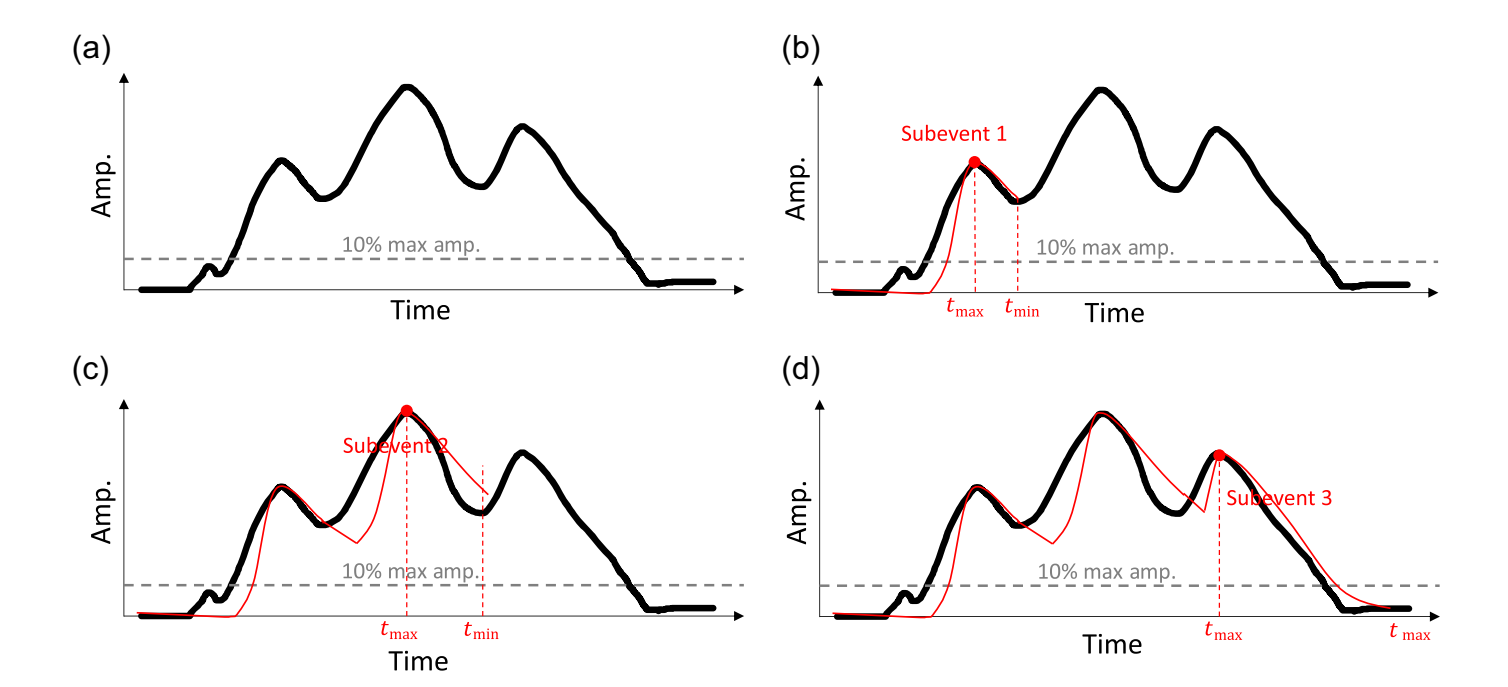
which has a plateau at frequencies much lower than  $f_c$  and decreases proportional to  $f^2$  at frequencies higher than  $f_c$ . The stress drop  $\Delta \sigma$  is proportional to  $f_c^3$  (Madariaga, 1976).

We call the Brune source that best matches the STF of an earthquake  $\Omega_{\rm STF}$ . The seismic moment and corner frequency of  $\Omega_{\rm STF}$  are  $M_{\rm STF}$  and  $f_{\rm STF}$ , respectively. To determine  $M_{\rm STF}$  and  $f_{\rm STF}$  we transform the SCARDEC STF to the frequency domain using a fast Fourier transform algorithm (Cooley and Tukey, 1965) and estimate  $f_{\rm STF}$  in the frequency range of 0.01–2.0 Hz using the trust-region-reflective least-squares algorithm (Branch *et al.*, 1999). For a complex STF with multiple maxima,  $M_{\rm STF}$  approximates the earthquake's integrated moment rate, and  $f_{\rm STF}$  represents an average value of the rupture duration.

To model a complex STF with multiple episodes of high moment rate (i.e., multiple subevents), we write the STF as a sum of Brune pulses:

$$\Omega_{\text{sum}}(t) = \sum_{N=1}^{N_{\text{ev}}} \Omega_N(t, t_N, f_N, M_N).$$
 (3)

To determine the number of resolvable Brune pulses in  $\Omega_{\text{sum}}$ , we follow the iterative approach by Danré et al. (2019) with some modifications (Fig. 1). There are three essential steps: (1) To determine subevent N, find the time  $t_{\text{MAX}}$  of the N local maximum in the STF that is larger than 10% of the STF's maximum value to avoid overfitting small oscillations as individual subevents. Then we find the time  $t_{\rm MIN}$  of the first local minimum in the STF more than 0.5 s after  $t_{\text{MAX}}$ , to avoid overfitting oscillations close to each other as individual subevents. This requirement should not affect the number of subevents because 0.5 s is only about 10% and 1% of the rupture duration of  $M_{\rm w}$  5.5 and 8 earthquakes. (2) Find the seismic moment  $M_N$  and corner frequency  $f_N$  of subevent N that minimize the least-squares difference between the STF and  $\Omega_{\text{sum}} =$  $\sum_{k=1}^{N} \Omega_k(t, t_k, f_k, M_k)$  in the time range  $[0, t_{\text{MIN}}]$ . (3) Repeat steps (1) and (2) gradually adding subevents to  $\Omega_{\text{sum}}$  until the last subevent  $N_{\rm ev}$ . We normalized the STFs such that the total integrated area is 1.0 and calculated the residual curve between the STF and  $\Omega_{\text{sum}}$ . We then calculated the integrated



area of the residual curve to obtain the misfit. We discard STFs if the misfit is larger than 0.5. Analogous to the estimate of  $M_{\rm STF}$  and  $f_{\rm STF}$ , we define  $M_{\rm sum}$  and  $f_{\rm sum}$  as the seismic moment and corner frequency of a single Brune pulse that best matches  $\Omega_{\rm sum}$  in a least-squares sense.

# METHOD: DERIVING STF USING TWO BRUNE PULSES

We derive for the first time the STFs and source spectra of earthquakes with multiple subevents whose spectra are described by the Brune model. We focus on earthquakes with two subevents. As shown in the Analysis of SCARDEC STFs section, two-subevents earthquakes account for 43% of the SCARDEC data set. The expression of STFs can also be extended to earthquakes with three or more subevents. We write the STF of an earthquake with two subevents as

$$\Omega_{\text{sum}}(t) = \Omega_L(t, t_L, f_L, M_L) + \Omega_S(t, t_S, f_S, M_S), \tag{4}$$

in which the parameters  $t_L$ ,  $f_L$ , and  $M_L$  and the parameters  $t_S$ ,  $f_S$ , and  $M_S$  are the onset times, corner frequencies, and seismic moments of the large and small subevents  $\Omega_L$  and  $\Omega_S$ , respectively. The power spectrum of  $\Omega_{\rm sum}$  for two pulses is

$$\Omega_{\text{sum}}^{2}(f) = \frac{M_{L}^{2}}{k_{L}^{2}} + \frac{M_{S}^{2}}{k_{S}^{2}} + \frac{2M_{S}M_{L}}{k_{S}k_{L}}\cos\{2\pi f(t_{L} - t_{S}) + \alpha_{L} - \alpha_{S}\}, (5)$$

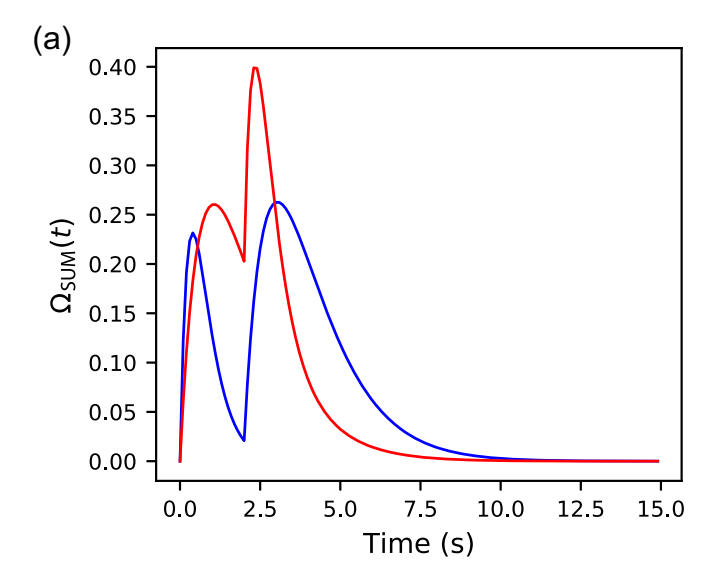
in which  $k_L=1+f^2/f_L^2$ ,  $k_S=1+f^2/f_S^2$ ,  $\sin^2\alpha_L=(k_L-1)/k_L$ , and  $\sin^2\alpha_S=(k_S-1)/k_S$ . The first and second terms in equation (5) are Brune spectra with different low-frequency plateaus and corner frequencies that determine the onset of the spectral fall off. The third term represents oscillations in the spectrum with periods determined by T and the

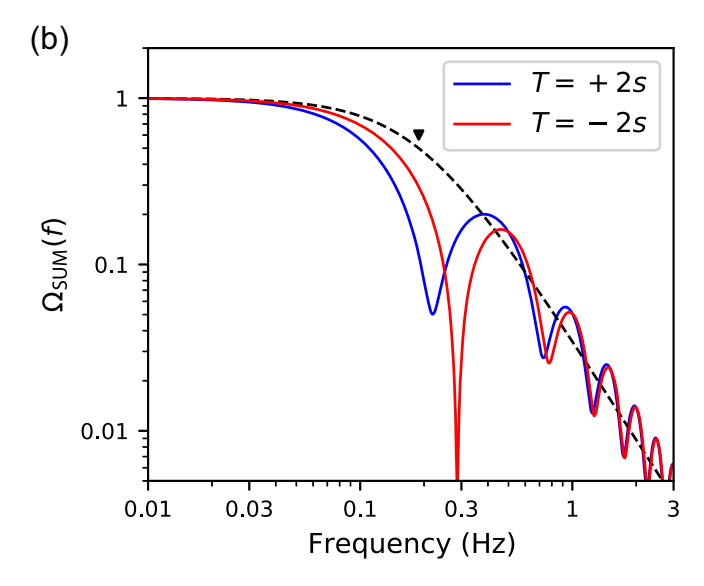
**Figure 1.** Flowchart of STF decomposition. (a) Set 10% of the maximum amplitude as the water level, below which pulses would not be fitted. (b) Fit the first pulse to subevent 1. The time of the maximum amplitude  $(t_{\rm MAX})$  is also the peak time of subevent 1. The time of minimum amplitude  $(t_{\rm MIN})$  after the pulse is the end boundary of calculating misfit. (c) Fit the second pulse to subevent 2.  $t_{\rm MAX}$  and  $t_{\rm MIN}$  are updated accordingly. (d) Fit the last pulse to subevent 3.  $t_{\rm MIN}$  is updated as the end of time. The color version of this figure is available only in the electronic edition.

phase shifts determined by  $f_L$  and  $f_S$ . We reduce the number of free parameters to four by considering the moment ratio  $M = M_L/M_S$  and the onset time difference  $T = t_L - t_S$  of the largest and smallest subevents instead of  $M_L, M_S, t_L$ , and  $t_S$  individually.

Figure 2 illustrates the typical form of  $\Omega_{sum}$  in the time (Fig. 2a) and frequency (Fig. 2b) domains.  $\Omega_{\text{sum}}$  has two subevents with corner frequencies  $f_L = 0.15 \text{ Hz}$  and  $f_s = 0.40 \text{ Hz}$  and a moment ratio M = 3. We consider T = -2 s and T = +2 s for which the large subevent precedes and succeeds the small subevent by two seconds, respectively (Fig. 2a). The order of the small and the large subevent can significantly change the shape of the STF and its peak values. For example, when T = -2 s, the two maxima in the STF are similar, but for T = +2 s, the second maximum is 60% higher than the first one. The spectra for T = -2 s and T = +2 s have local minima at different frequencies, and they converge and decay approximately proportional to  $f^2$  at frequencies higher than about 0.5 Hz (Fig. 2b). The Brune pulse that optimally fits  $\Omega_{\text{sum}}$  has a corner frequency  $f_{\text{sum}} = 0.19$  Hz for both T = -2 s and T = +2 s, about two times lower than  $f_s$ . The location of the first spectral minimum and the spectral decay at high frequencies depend on the values of  $f_L$ ,  $f_S$ , M, and T.

Figure 3a shows how  $f_{\text{sum}}$  varies as a function of T and M for ranges we resolve for the majority of STFs in the SCARDEC





catalog with two subevents. As in Figure 2,  $f_L$  is 0.15 Hz and  $f_S$  is 0.40 Hz. For high values of M,  $f_{\rm sum}$  approaches  $f_L$  because the largest of the two subevents dominates  $\Omega_{\rm sum}$ . For values of M near 1 and for T near 0,  $f_{\rm sum}$  is intermediate between  $f_L$  and  $f_S$ . The asymmetry of  $f_{\rm sum}$  about T=0 indicates that  $f_{\rm sum}$  depends on the order of the large and small subevents in the STF, especially when the onset time difference between the subevents is small. The asymmetry originates from a phase shift of  $2(\alpha_L - \alpha_S)$  when the sign of T changes (see equation 5), which is the strongest when M is high. Figure 3b shows how  $f_{\rm sum}$  varies with subevent corner frequencies  $f_L$  and  $f_S$ . We find that  $f_{\rm sum}$  is more related to  $f_L$  than  $f_S$  when M=3 and T=2.  $f_{\rm sum}$  is closer to the smaller one of  $f_L$  and  $f_S$  and increases with either of them.

events have corner frequencies of 0.15 and 0.40 Hz, respectively. The moment ratio  $M=M_L/M_S=3$ . In cases 1 (red) and 2 (blue), the largest pulse is the first and second in the sequence so T=-2 s and T=+2 s, respectively. (b) Amplitude spectra (solid lines) of the STFs with corresponding colors shown in panel (a). The dashed line is the spectrum of a single-pulse Brune source that best matches  $\Omega_{\rm sum}$  in a least-squares sense. They are virtually the same for T=-2 s and T=+2 s. The corner frequency of this Brune source is  $f_{\rm sum}=0.19$  Hz. The color version of this figure is available only in the electronic edition.

**Figure 2.** (a)  $\Omega_{\text{sum}}$  for a sum of two Brune pulses. The large and small sub-

## **ANALYSIS OF SCARDEC STFs**

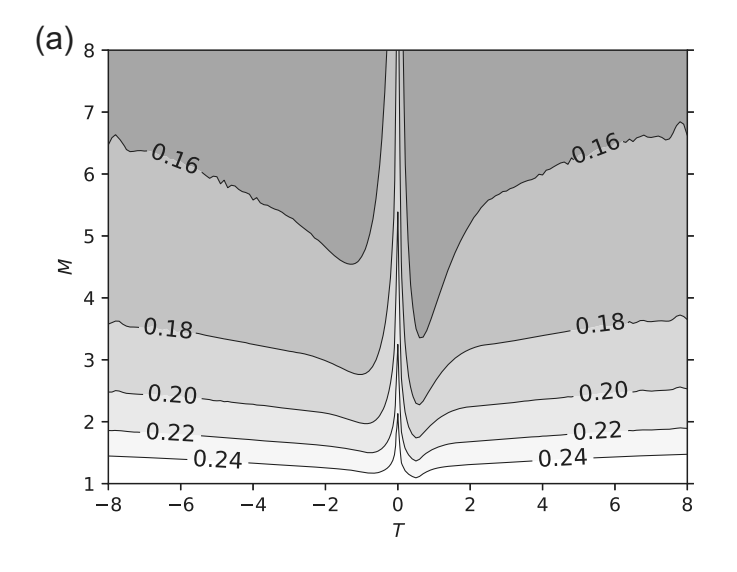
The SCARDEC catalog with source information of hundreds of earthquakes facilitates our exploration. Although it does not include constraints on fault slip distribution such as the finite-fault modeling databases developed by Ye et al. (2016) and Hayes (2017), it is an order of magnitude larger. The SCARDEC analysis is based on the analysis of the waveforms of the teleseismic body-wave phases P, PcP, PP, ScS, and SH and their surface reflected phases to maximize the range of wave take-off angles in the analysis and thus resolution. There are no simplifications regarding the spatial-temporal complexity of the rupture process, so differences of the STFs at different stations may capture rupture directivity. However, we use the average of the STFs from all stations as an estimate of the overall time dependence of moment rate. The SCARDEC catalog has been used in determining the variations of strain drop, stress drop, and radiated energy with depth, magnitude, and tectonic settings (Vallée, 2013; Courboulex et al., 2016; Chounet and Vallée, 2018; Denolle,

2019; Yin et al., 2021), as well as inversions for rupture velocity

We decompose STFs of  $M_{\rm w}$  5.5–8.0 earthquakes between 1992 and 2017 in the SCARDEC catalog. Out of 3348 earthquakes, 1640 earthquakes (49%) have two or more subevents. Danré *et al.* (2019) identified a higher percentage of earthquakes with multiple subevents (81%) most likely because the Gaussian model describes the source with three free parameters in contrast to the two free parameters in the Brune model. Nevertheless, both studies indicate that at least half of moderate-to-large earthquakes are complex.

As an example, Figure 4a,c shows the reconstructed STFs (i.e.,  $\Omega_{\text{sum}}$ ) and the original STFs of the 8 December 2017  $M_{\rm w}$  6.2 earthquake in Caroline Islands and of the 25 December 2016  $M_{\rm w}$  7.6 earthquake in southern Chile. Figure 4b,d shows their spectra  $\Omega_{STF}$  and  $\Omega_{sum}$ . For the Caroline Islands earthquake, we determine that  $\Omega_{\text{sum}}$  is a sum of two Brune sources with a moment ratio of 5.75 and with corner frequencies of 0.13 Hz ( $f_L$ ) and 0.30 Hz ( $f_S$ ). The large subevent occurred 2.3 s after the small subevent. The misfit between the normalized STF and  $\Omega_{\text{sum}}$  is 32.8%. The corner frequency is inferred to be 0.11 Hz, slightly lower than  $f_L$ , because the largest subevent represents more than 85% of the total moment. The observed and synthetic STFs release 90% of the total moment at 6.6 and 7.8 s. The southern Chile earthquake is also decomposed into two Brune sources although it has a longer source duration. For this event, the

and rupture direction (Chounet et al., 2018).



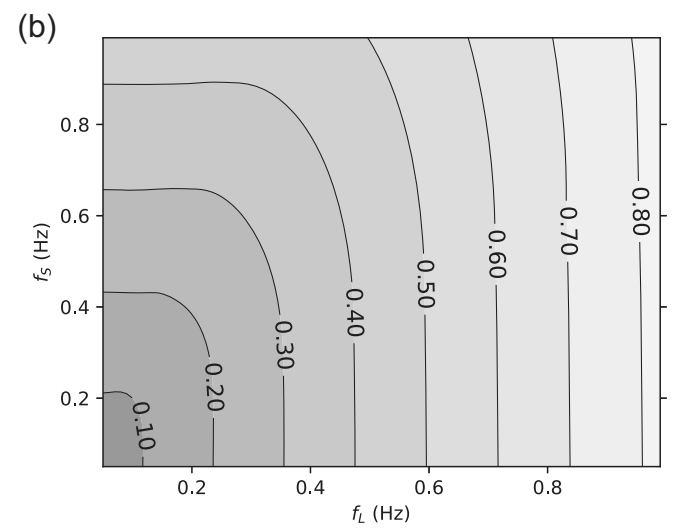


**Figure 3.** (a) Contour plot of the corner frequency  $f_{\text{sum}}$  as a function of T and M. The subevent corner frequencies are  $f_L = 0.15$  Hz and  $f_S = 0.40$  Hz.

(b) Contour plot of  $f_{\rm sum}$  as a function of  $f_L$  and  $f_S$ . The moment ratio and onset time difference of the two subevents are T=2 s and M=3.

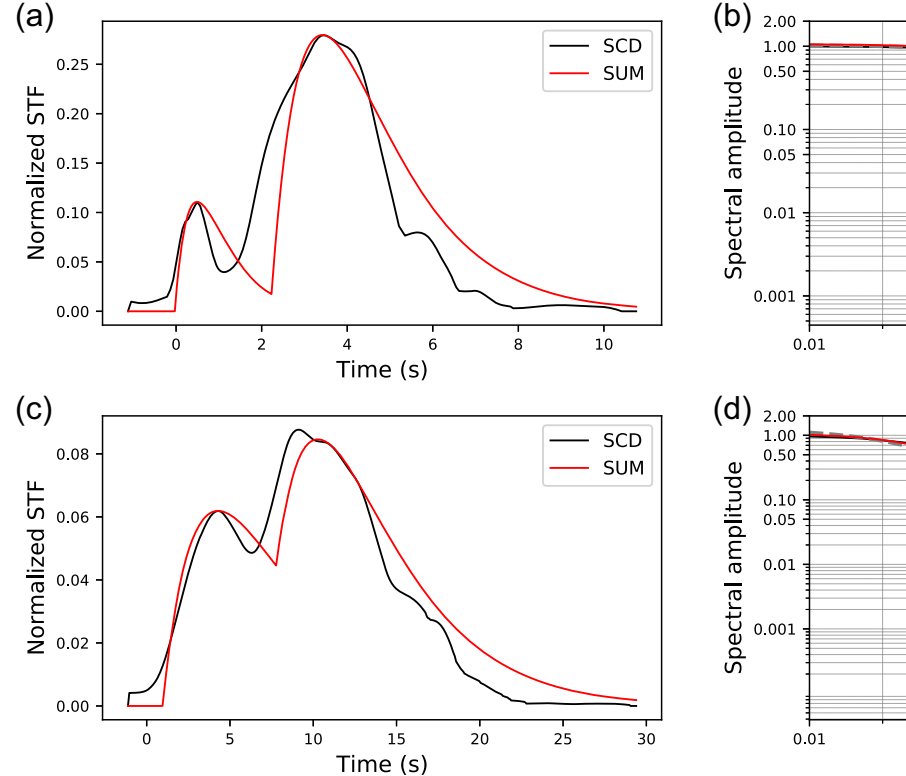
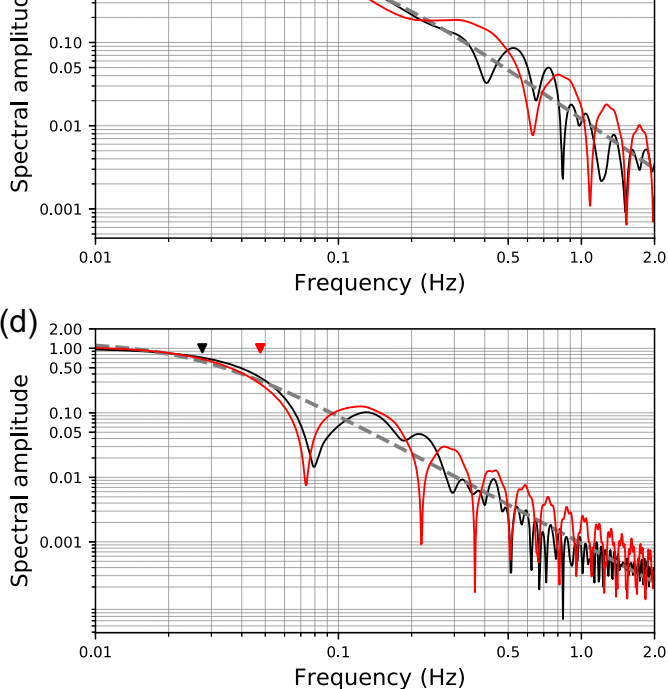
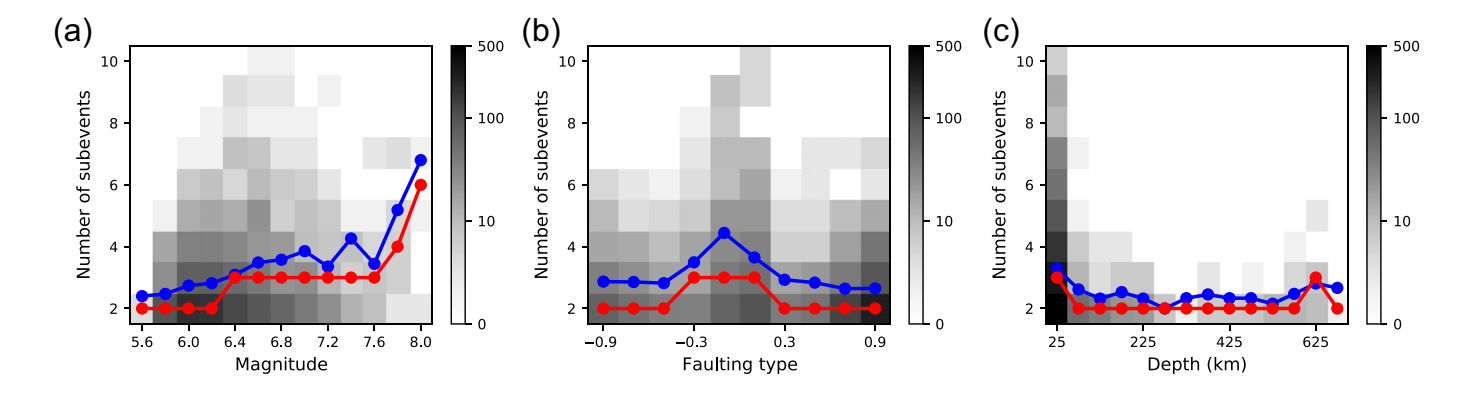


**Figure 4.** (a) Normalized STFs of the Caroline Islands  $M_{\rm w}$  6.2 earthquake on 8 December 2017 from the seismic source characteristic retrieved from deconvolving teleseismic body waves (SCARDEC) data set (black line) and the best-fitting sum  $\Omega_{\rm sum}$  of two Brune subevents (red line). (b) The spectra of the STF (black line),  $\Omega_{\rm STF}$  (dashed line), and  $\Omega_{\rm sum}$  (red line). The corner frequency  $f_{\rm STF}=0.11$  Hz is marked by a black reversed triangle.



The corner frequencies  $f_L=0.13$  Hz and  $f_S=0.30$  Hz are marked by red reversed triangles. (c,d) same as panels (a) and (b), but for the  $M_{\rm w}$  7.6 southern Chile earthquake of 25 December 2016, with corner frequencies  $f_{\rm STF}=0.028$  Hz,  $f_L=0.048$  Hz, and  $f_S=0.048$  Hz and M=1.08. The color version of this figure is available only in the electronic edition.



onset time difference T=+6.82 s, and the moment ratio M=1.08 with a misfit of 18.7%. The corner frequencies  $f_L$  and  $f_S$  are both 0.048 Hz and much larger than the inferred earthquake corner frequency (0.028 Hz) because the two subevents have similar moments. The observed and synthetic STFs release 90% of the total moment at 17.0 and 19.3 s, respectively. The synthetic source duration is larger than the observed source duration because the fixed Brune STF decreases more slowly than the observed STF. Compared to Figure 4d, spectra in Figure 4b have an extra plateau at 0.2–0.3 Hz because of the large difference between  $f_L$  and  $f_S$ .

Figure 5 summarizes how the number of subevents varies with moment magnitude, focal mechanism, and source depth. It suggests that the number of subevents increases with moment magnitude in the range of 5.5-8.0 (Fig. 5a) and that strike-slip earthquakes are more complex than dip-slip earthquakes (Fig. 5b). Earthquakes that have eight or more subevents are all strike-slip earthquakes. This is in agreement with the previous study by Danré et al. (2019), indicating that the correlation of source complexity with magnitude and faulting type, as quantified by the number of subevents, is a robust characteristic of the SCARDEC catalog and weakly influenced by the assumed source model for the subevent. We also find that shallow (<50 km) and very deep (>600 km) earthquakes have more subevents than earthquakes between 50 and 600 km depth (Fig. 5c). Patterns in Figure 5b,c are also observed in Yin et al. (2021).

#### **SCARDEC STFs WITH TWO SUBEVENTS**

From the 1640 multisubevent STFs in the SCARDEC catalog, 714 STFs (43%) have two subevents, more than the sum of the number of earthquakes with three (361), four (198), and five (104) subevents. Because two-subevent earthquakes are most common and the simplest scenario of complex earthquakes, our analysis focuses on earthquakes with two subevents.

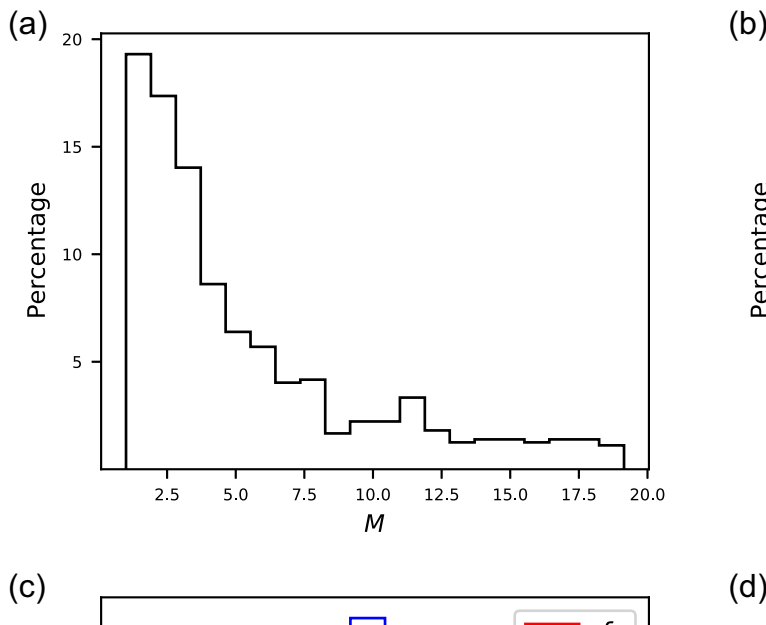
The magnitude range of two-subevent earthquakes is  $M_{\rm w}$  5.7–8.0. The ratio M is lower than 8 for about 75% of the STFs (Fig. 6a) and the absolute onset time difference T is between 2.0 and 8.0 s for about 80% of the STFs (Fig. 6b). T is negative for 521 STFs, suggesting that if small subevents before and after larger ones are equally detectable the largest

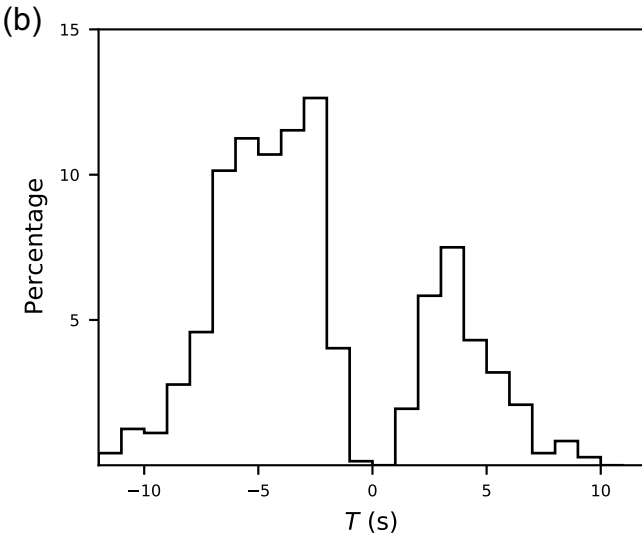
**Figure 5.** Contour plot of the number of earthquakes. The *y*-axis shows the number of subevents in the STF up to 10. The *x*-axis indicates the earthquake's (a) moment magnitude, (b) faulting type, and (c) focal depth. The values of faulting type range from -1 (normal faulting) to 0 (strike-slip faulting) to +1 (reverse faulting) following the quantification by Shearer et al. (2006). The blue and red circles signify means and medians determined for bins of  $\pm 0.1$  (moment magnitude),  $\pm 0.1$  (faulting type), and  $\pm 25$  km (focal depth). The color version of this figure is available only in the electronic edition.

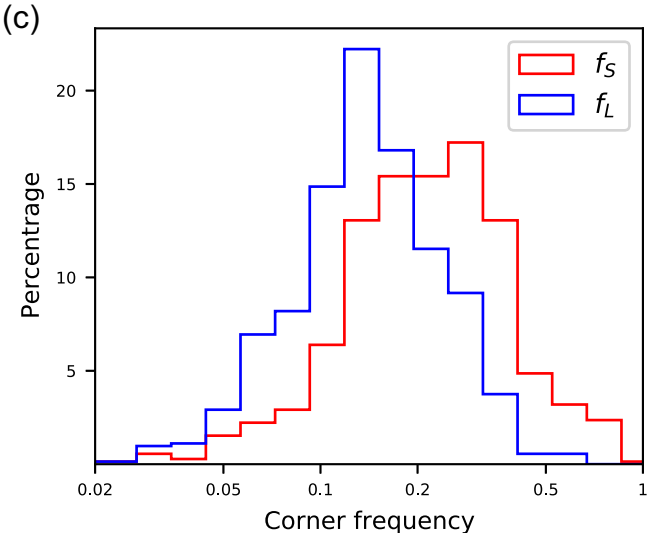
subevent precedes the smallest subevent more often. The corner frequency  $f_L$  of the large subevent has a median value of 0.14 Hz, higher than the corner frequency  $f_S$  of the small subevent that has a median of 0.21 Hz (Fig. 6c), consistent with the common observation that smaller events have higher corner frequencies.  $f_L/f_S$  has a median of 0.65 (Fig. 6d), with 76% of values smaller than 1.0, which is consistent with the common observation that smaller events tend to have higher corner frequencies.

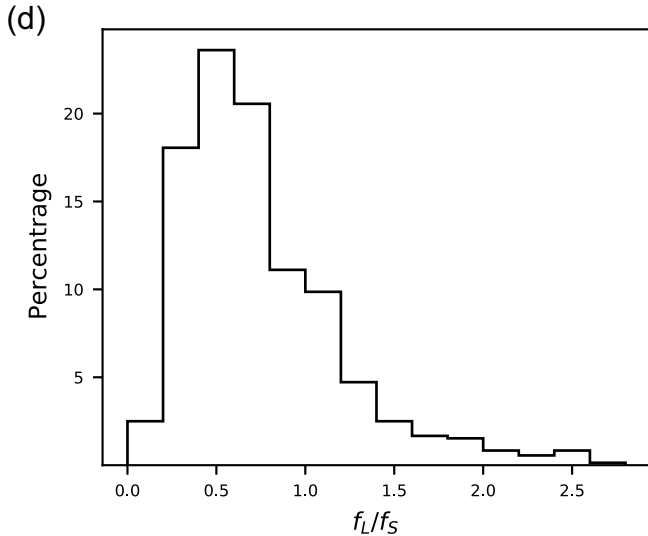
In Figure 7, we evaluate the significance of the corner frequency  $f_{\rm STF}$  of the 714 SCARDEC STFs that are decomposed to have two subevents. The correlation between  $f_{\rm STF}$  and  $f_L$  (Fig. 7b,d) is higher than the correlation between  $f_{\rm STF}$  and  $f_S$  (Fig. 7a,c) with cross-correlation coefficients of about 0.90 and 0.57, respectively. This indicates that the large subevent determines  $f_{\rm STF}$  the most, which agrees with the theoretical results shown in Figure 2b. We find that the corner frequencies of subevents  $f_S$  and  $f_L$  are overall higher than the earthquake corner frequency  $f_{\rm STF}$ . The correlations between  $f_{\rm STF}$  and subevent corner frequencies further supports the finding of Danré *et al.* (2019) that the moment of subevents is correlated to the moment of the main event for self-similar earthquakes.

The color coding in Figure 7a,b indicates that with increasing moment ratio M, the difference between  $f_{\rm STF}$  and  $f_{\rm S}$  tends to increase, whereas the difference between  $f_{\rm STF}$  and  $f_{\rm L}$  tends to decrease, which is also observed in Figure 2a. The plot of the  $f_{\rm S}/f_{\rm STF}$  and  $f_{\rm L}/f_{\rm STF}$  ratios in Figure 8a further illustrate this. The limitation in frequency bandwidth could result in increasing  $f_{\rm S}/f_{\rm STF}$  with M if  $f_{\rm S}$  is high enough, but here most corner frequency estimates are within 0.7 Hz, which should be









resolvable given a time step of 0.005 s. Beginning with a similar spread at M=1, the scatter in  $f_S/f_{\rm STF}$  increases with increasing M, whereas  $f_L/f_{\rm STF}$  tends to cluster to a value of about 1.2. Although  $f_L/f_{\rm STF}$  is expected to approach 1 theoretically for the highest values of M, we suspect that the misfit of the decomposition of STF renders  $\Omega_{\rm sum}$  to have a slightly different frequency content than  $\Omega_{\rm STF}$ . Figure 7c,d shows that for an increasing absolute onset time difference |T| between subevents,  $f_{\rm STF}$  and  $f_L$  decreases. This is consistent with the fact that |T| controls the total source duration, which is inversely proportional to the corner frequency of the Brune pulse. Therefore,  $f_{\rm STF}$  and the closely correlated  $f_L$  are inversely proportional to |T|, whereas the change of  $f_S$  with |T| is less obvious due to high scatter.

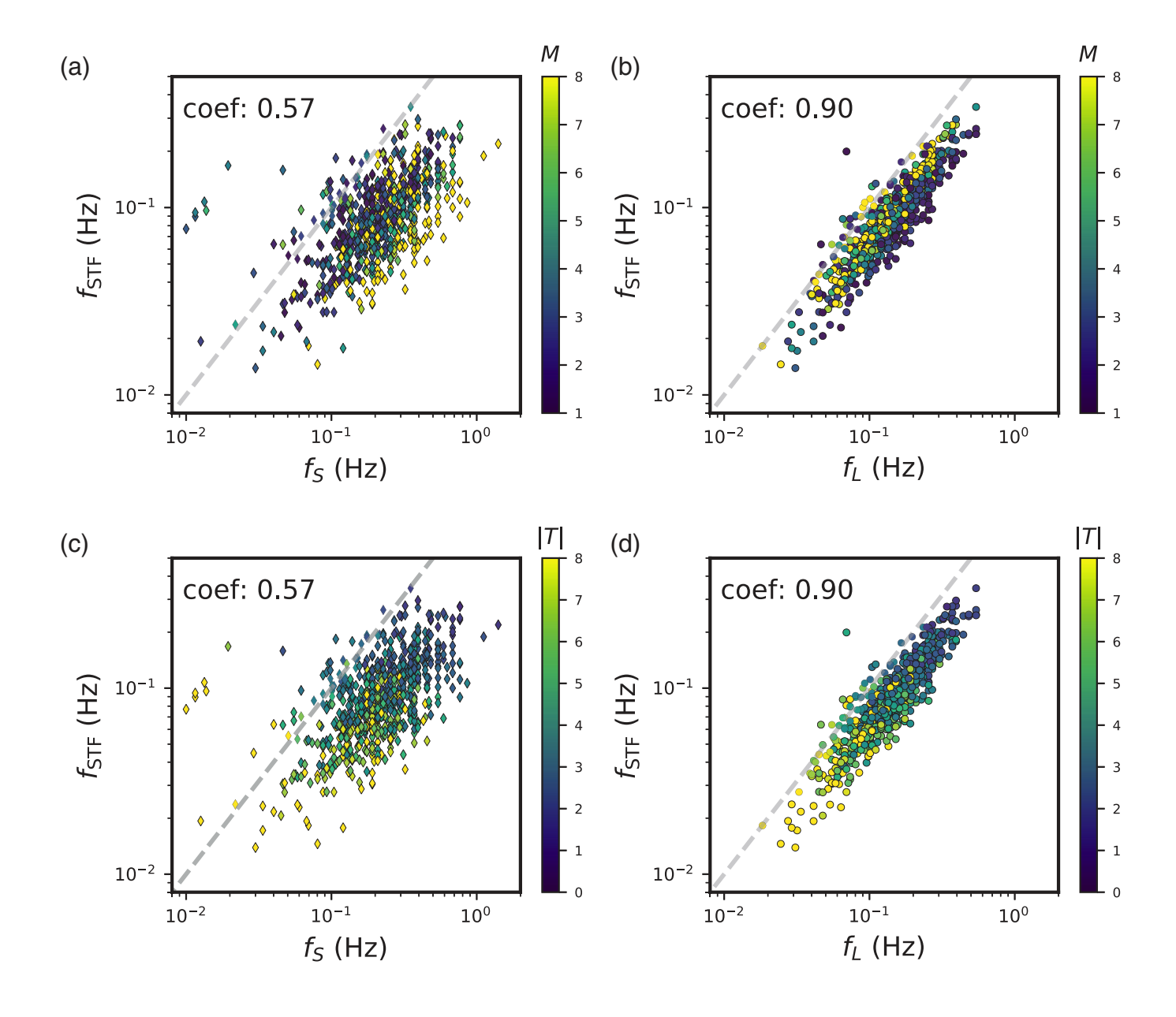
**Figure 6.** Histograms of (a) moment ratio  $= M_L/M_S$ , (b) onset time difference  $T = t_L - t_S$ , (c) corner frequency of the largest subevent  $f_L$  and of the smallest subevent  $f_S$ , and (d) ratio of  $f_L$  to  $f_S$  for 714 STFs with two subevents in the SCARDEC catalog. The color version of this figure is available only in the electronic edition.

Figure 8b shows an asymmetry in the ratios  $f_S/f_{STF}$  and  $f_L/f_{STF}$  with reference to T=0, implying that the order of the large and small subevents of subevent (i.e., T>0 and T<0) has an influence on the corner frequency estimates. The variation in  $f_S/f_{STF}$  for T<0 is two times higher than for T>0, suggesting that  $f_S$  is similar to  $f_{STF}$  and better constrained

if the small subevent precedes that large subevent. The variation in ratio  $f_L/f_{\rm STF}$  does not change with T, but the mean value of  $f_L/f_{\rm STF}$  for T <0 is slightly smaller than  $f_L/f_{\rm STF}$  for T >0 (1.60 versus 1.79). Because the absolute value of T is higher than 1 for most STFs in the SCARDEC catalog (see Fig. 6b), the relatively small influence of T on  $f_L/f_{\rm STF}$  is consistent with Figure 2a, where we found that  $f_{\rm STF}$  depends strongly on T only when |T| < 1.

The Brune model relates the corner frequency  $f_c$  to stress drop  $\Delta \sigma$  assuming a circular crack model:

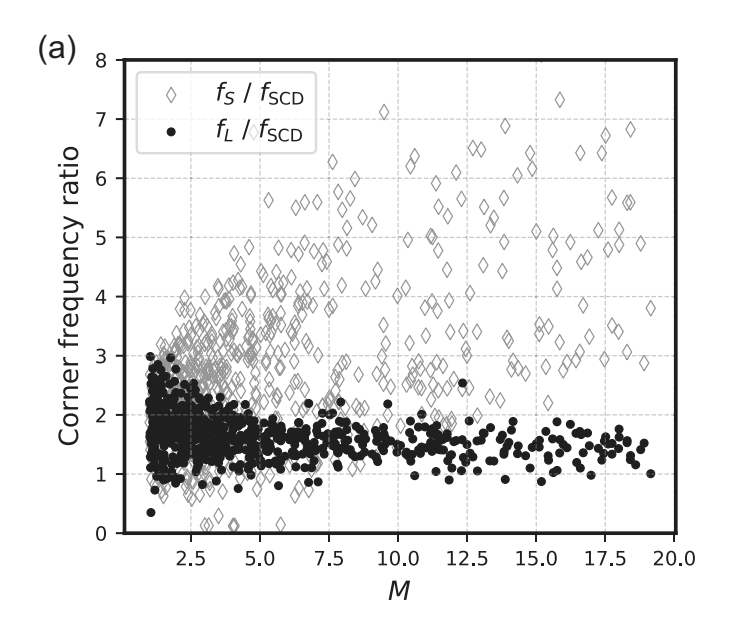
$$\Delta\sigma = \frac{7M_0 f_c^3}{16\beta^3 k^3}.$$
(6)

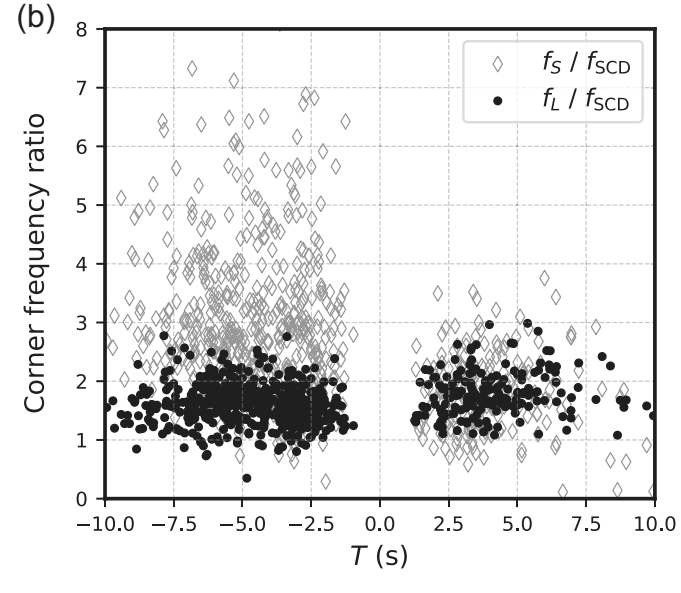


Here k is a constant and  $\beta$  is the shear-wave velocity (Madariaga, 1976). In equation (6),  $\Delta \sigma$  represents the average stress change on the fault plane. Analogous to our definitions for  $f_{\rm STF}$ , we define  $\Delta\sigma_{\rm STF}$  as the average stress drop determined for the SCARDEC STF. Further, we define  $\Delta \sigma_L$  and  $\Delta \sigma_S$  and  $M_L$ and  $M_S$  as the stress drops and seismic moments of the large and small subevents, respectively. The shear-wave velocity is referred from PREM (Dziewonski and Anderson, 1981) model. We assume the rupture velocity is about  $0.7\beta$  (Ye et al., 2016; Hayes, 2017; Chounet et al., 2018). The value of k is related to the spherical average of the corner frequency and is different for P and S waves (Sato and Hirasawa, 1973; Madariaga, 1976; Kaneko and Shearer, 2014, 2015; Wang and Day, 2017). Because SCARDEC STFs are obtained by averaging *P* and *S* waves after removal of Green's functions, we set k as 0.32 according to Sato and Hirasawa (1973) and Kaneko and Shearer (2015).  $\Delta \sigma_{STF}$ ,  $\Delta \sigma_L$ , and  $\Delta \sigma_S$  are proportional to the cube of  $f_{STF}$ ,  $f_L$ , and

**Figure 7.** (a,b) The corner frequency  $f_{\rm STF}$  as a function of the corner frequency  $f_{\rm S}$  and  $f_{\rm L}$  color coded by moment ratio M. (c,d) The corner frequency  $f_{\rm STF}$  as a function of the corner frequency  $f_{\rm S}$  and  $f_{\rm L}$  color coded by absolute onset time difference |T|. The dashed lines indicate a 1:1 correlation. The color version of this figure is available only in the electronic edition.

 $f_S$ . Therefore, as for  $f_L$ ,  $f_S$ , and  $f_{STF}$ , the correlation between  $\Delta\sigma_{STF}$  and  $\Delta\sigma_L$  is higher than the correlation between  $\Delta\sigma_{STF}$  and  $\Delta\sigma_S$  (Fig. 9a). The correlation of Brune stress-drop estimates with the largest asperity supports the usage of the moment-weighted stress drop and the energy-based stress drop (Noda *et al.*, 2013).  $\Delta\sigma_L$  and  $\Delta\sigma_S$  are also larger than  $\Delta\sigma_{STF}$  (Fig. 9b). For 50% of the STFs  $\Delta\sigma_L$  and  $\Delta\sigma_S$  are larger than  $\Delta\sigma_{STF}$  by a factor of 4, and stress drops of the small subevents is an order of magnitude higher than the overall stress drop for 20% of the earthquakes in the SCARDEC catalog (see also Fig. 6c).





# COMPARISON WITH FINITE-FAULT INVERSION RESULTS

Through the STFs decomposition, we find that the corner frequency of the master event is more related to the largest subevent. STFs show temporal behavior of the rupture moment release, but, however, provide no spatial information of the rupture process. Thus, we compare subevent corner frequencies measured from STFs with rupture dimensions of subevents estimated from finite-fault inversion data sets. Ye et al. (2016) applied finite-fault inversion to teleseismic P waveforms of 114 earthquakes larger than  $M_{\rm w}$  7.0. We fit the source spectra of STFs from finite-fault inversion to the Brune source model to estimate the corner frequency of the earthquake  $f_{\rm STF}$  and convert it to rupture radius following  $r_{STF} = k\beta/f_{STF}$ , in which k is a constant and  $\beta$  the shear-wave velocity. Assuming an average crustal shear-wave velocity ( $\beta = 3.5 \text{ km/s}$ ), the rupture velocity used by Ye et al. (2016) (2.5 km/s) is 70% of the shear-wave velocity. We use corresponding k values of P waves from Sato and Hirasawa (1973) and Kaneko and Shearer (2015). We then decompose STFs to estimate the moment of the largest subevent. Assuming that the largest subevent with the highest slip can be approximated by a circle, we use the moment release distribution to find the radius  $r_{\text{FNT}}$  when the total moment release within the circle is equal to the largest subevent. As an example, Figure 10a,b displays the STF for the 18 April 2014 Guerrero earthquake and its slip map where the circle with a radius of  $r_{\text{FNT}} = 24$  km outlines the region of slip of the largest subevent.

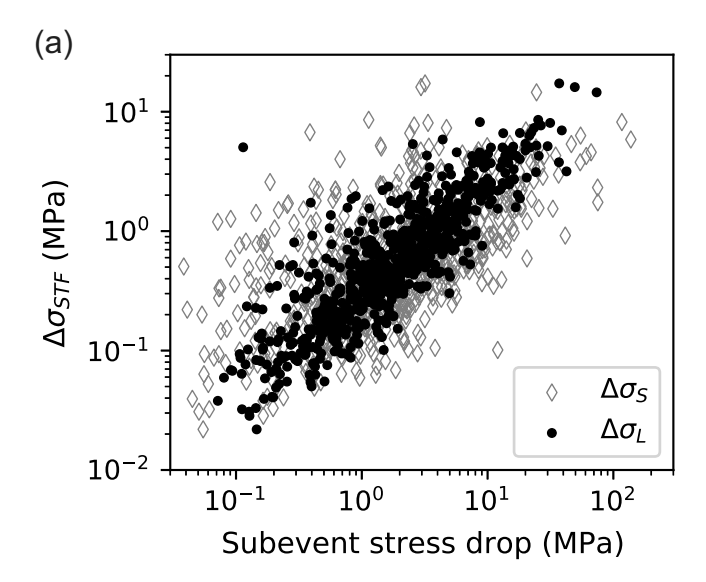
Figure 10c,d shows that  $r_{\rm STF}$  is positively correlated with  $r_{\rm FNT}$ . The radius  $r_{\rm STF}$  depends linearly on k. For k=0.23 (Sato and Hirasawa, 1973)  $r_{\rm STF}$  is about 30% higher than for k=0.32 (Kaneko and Shearer, 2015), but k has no influence on the correlation between  $r_{\rm STF}$  and  $r_{\rm FNT}$ . A change of 10% moment would result in approximate 10% change of the radius. The estimation of  $r_{\rm FNT}$  is rough because the rupture

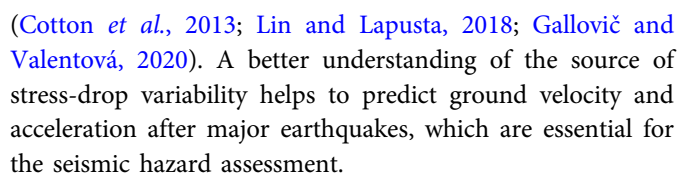
**Figure 8.** The ratio between corner frequencies  $f_L$  (solid black circles) and  $f_S$  (gray open diamonds) to  $f_{STF}$  as a (a) function of moment ratio M (b) and onset time difference T.

areas of subevents may not be circles. Nevertheless, the proportionality of  $r_{\rm STF}$  and  $r_{\rm FNT}$  supports our conclusion that the largest subevent strongly influences estimates of the earthquake corner frequency and rupture dimension and estimates of earthquake corner frequency represent rupture dimensions of the largest subevent.

#### **INDICATION ON STRESS-DROP VARIABILITY**

Stress drops estimated from the SCARDEC STFs data set (i.e.,  $\Delta \sigma_{\rm STF}$  in Fig. 9a) have a standard deviation of about a factor of 3.5. This standard deviation is close to the factor-of-three variability of stress drop estimated from the SCARDEC STFs of nonstrike-slip earthquakes by Courboulex et al. (2016) and is similar to the variability of stress drop estimated from the moment rate functions of earthquakes in dynamic rupture simulations (Gallovič and Valentová, 2020). Allmann and Shearer (2009) obtained a stress-drop variability of about a factor of 4.5 using a spectral fitting method based on global numerical Green's functions. Our results show that the stress-drop variability may be a consequence of earthquake complexity. Whereas for a simple source, the stress drop inferred from the Brune source corner frequency represents the average stress drop on the fault plane, the stress drop of a complex rupture with multiple subevents is influenced strongly by the largest subevent. Therefore, earthquakes with the same magnitudes can have varying stress drops depending on the source complexity and the largest subevent dimension. This could explain the significant higher variability of stress drop estimated from STFs of simulated ruptures than the variability of stress drop prescribed in dynamic rupture models





In addition to the source complexity, the simplicity of the Brune source model itself can also lead to a systematic deviation of the stress-drop estimation. The Brune source model is widely applied due to its simplicity, but also suffers from inaccurate representation for complex earthquake sources. Although we obtain similar distributions of subevent numbers using the Brune source model as Danré *et al.* (2019) who used the Gaussian source model, the variation of stress-drop estimates is cubed when stress drop is converted from corner frequency estimates. Apart from the model choice, the quality of data set (Green's function removal in SCARDEC STFs), the frequency bandwidth, and the spectral fit method all contribute to the corner frequency and stress-drop variation.

### **APPLICATION TO SPECTRAL RATIOS**

Because the spectral ratio method is frequently used to estimate corner frequencies (e.g., Abercrombie, 2015; Huang et al., 2016; Uchide and Imanishi, 2016; Liu et al., 2020), we explore the resolution of the corner frequencies of a large earthquake (referred to as the master event hereafter) after dividing its spectrum  $\Omega_M$  by the spectrum  $\Omega_E$  of a collocated but smaller earthquake. The spectral ratio method isolates the source term of the master event, because for the same station the propagation and receiver effects are the same in  $\Omega_M$  and  $\Omega_E$ . Therefore, the smaller earthquake can be regarded as the empirical Green's function (referred to as eGf hereafter).

Assuming Brune sources as in equation (1), the spectral ratio is  $\Omega_{\text{ratio}}(f, f_{\text{ratio}}, M_{\text{ratio}}) = \Omega_M(f, f_M, M_M)/\Omega_E(f, f_E, M_E)$ , in which,  $M_M$ ,  $M_E$ ,  $f_M$ ,  $f_E$  are seismic moments and corner frequencies of the master event and the eGf. The spectral ratio

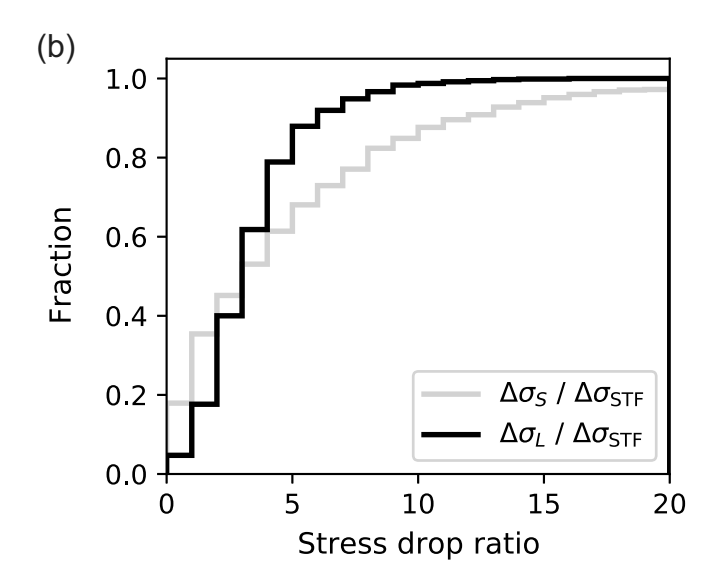
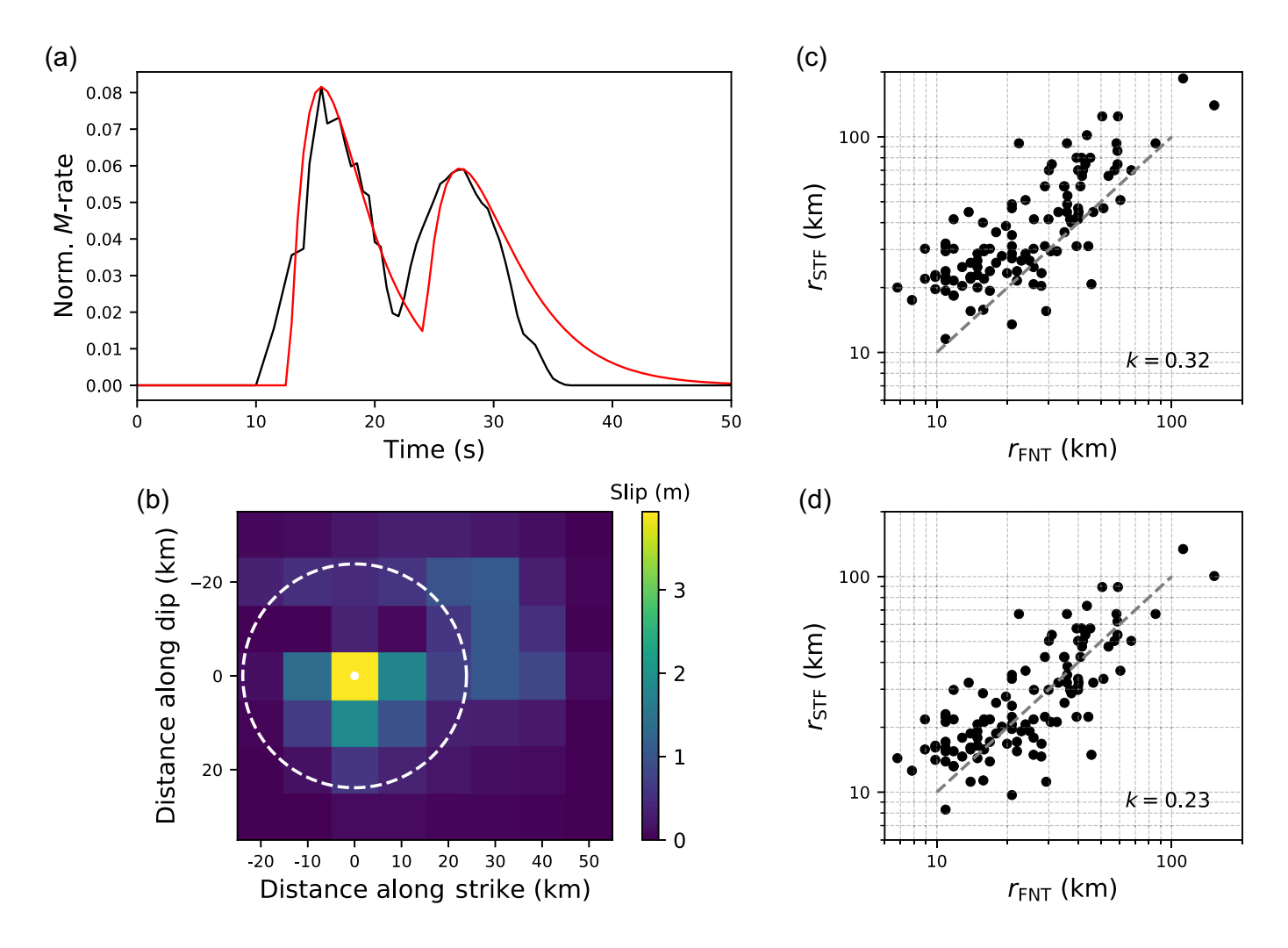


**Figure 9.** (a) Average stress drop  $\Delta\sigma_{\rm STF}$  as a function of the stress drop  $\Delta\sigma_L$  (circles) and  $\Delta\sigma_S$  (diamonds) of the large and small subevents, respectively. (b) Cumulative fraction of the ratios  $\Delta\sigma_L/\Delta\sigma_{\rm STF}$  (black line) and  $\Delta\sigma_S/\Delta\sigma_{\rm STF}$  (gray line).

 $\Omega_{\rm ratio}$  has a seismic moment ratio  $M_{\rm ratio}$  and a first corner frequency  $f_{\rm ratio}$  (i.e., master event corner frequency inferred from the spectral ratio method). The spectral ratio also has a second corner frequency that corresponds to the eGf corner frequency. If  $f_E$  is much higher than  $f_M$ ,  $\Omega_{\rm ratio}$  is equivalent to  $\Omega_M$  and  $f_M$  is equivalent to  $f_{\rm ratio}$ . If  $f_E$  is similar to  $f_M$ ,  $\Omega_{\rm ratio}$  decays more slowly at high frequencies than  $\Omega_M$ . There are two approaches to get the source spectral information  $M_M$  and  $f_M$ : (1) removing the Green's function and performing spectral fitting (e.g., Shearer *et al.*, 2006, 2019; Allmann and Shearer, 2007) and (2) fitting the spectral ratio of two Brune models based on empirical Green's function (e.g., Abercrombie, 1995, 2014, 2015), with two approaches benchmarked in Shearer *et al.* (2019).

We show the spectra and the spectral ratio of the second spectral ratio approach in Figure 11a. Figure 11c,d demonstrates this for the master events used in Figure 2 (i.e., events composed of two subevents with onset time difference of T = -2 s and T = +2 s) that have a corner frequency  $f_M = 0.19$  Hz for both cases of T. The eGfs used to compute  $\Omega_{\text{ratio}}$  are single-pulse Brune sources with corner frequencies of 0.5 Hz (Fig. 11c) and 1.5 Hz (Fig. 11d). In both cases,  $f_{\text{ratio}}$  is inferred to be lower than  $f_M$  because the first oscillation in the spectral ratios causes an earlier and faster decay near  $f_M$  (Fig. 2b). This decreasing effect on  $f_{\text{ratio}}$  is stronger when the eGf has a corner frequency closer to  $f_M$ . For  $f_E$  higher than 1 Hz,  $f_{\text{ratio}}$  approaches  $f_M$ asymptotically (Fig. 11b). In addition, the sequence of the large and small subevents affects  $f_{\text{ratio}}$ . The master event corner frequency is inferred to be larger when large subevent precedes small subevent (T = -2 s).



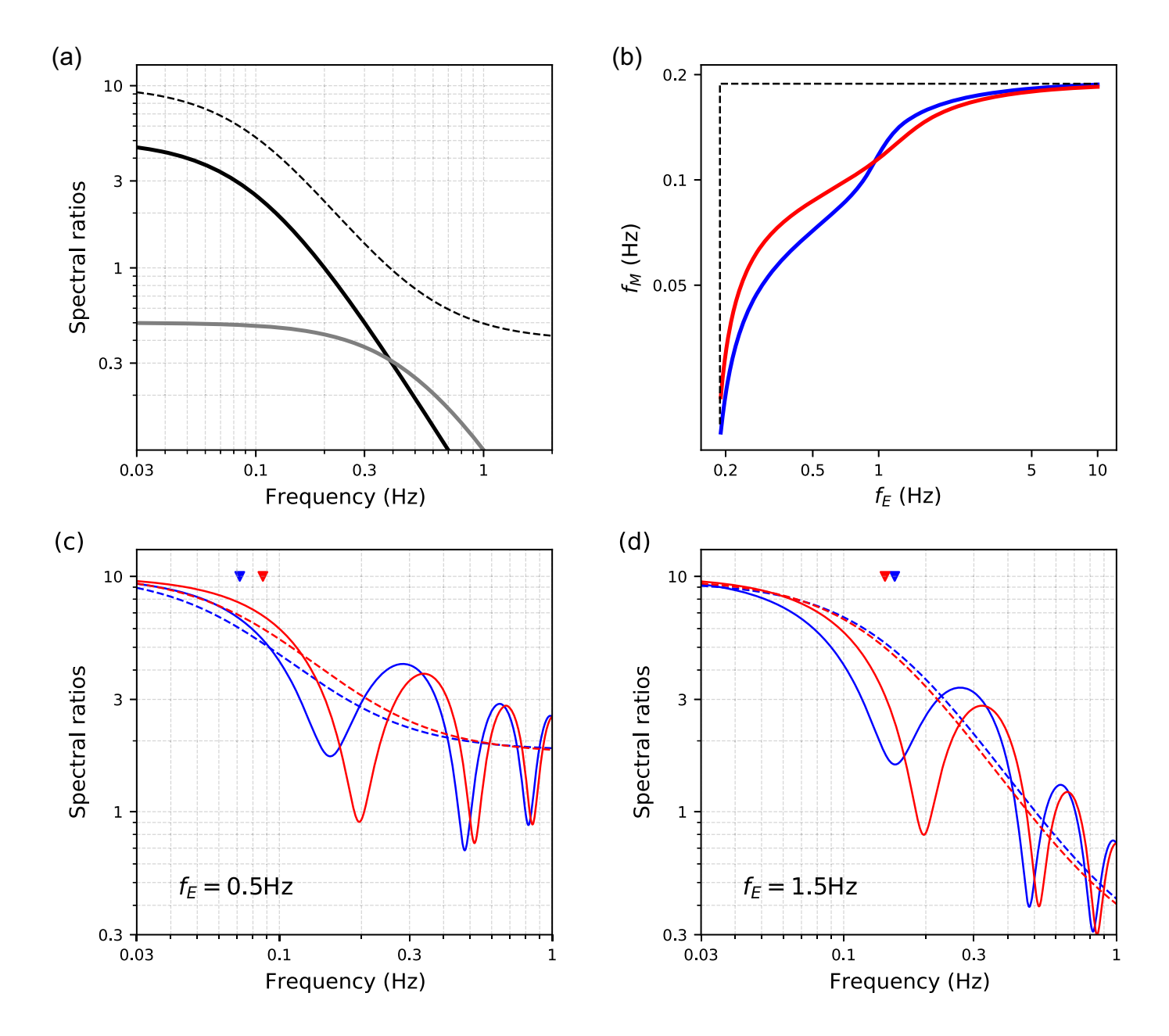
There is an upper bound of the frequencies (2 Hz in our case) in the source spectrum used for the fitting of the Brune source spectrum. Because  $\Omega_M$  and  $\Omega_E$  decay identically above  $f_E$ , the first corner of a spectral ratio is primarily determined by signals at frequencies lower than  $f_E$  that is usually smaller than the upper frequency range. For multisubevent earthquakes, oscillations at frequencies smaller than  $f_E$  dominate the modeling of spectral ratios. Theoretically, if the eGf has the form of a single-pulse Brune spectrum, its corner frequency does not strongly influence the estimate of the corner frequency of the master event. For complex master events, however, oscillations at frequencies smaller than  $f_E$ , rather than the overall fall-off, control the fitting. As  $f_E$  decreases, we are more likely to fit the first oscillation, which has a corner frequency smaller than the master event. Therefore, the spectral ratio method yields a larger variance in the estimated corner frequency than the direct fitting of earthquake source spectra when the master event consists of multiple subevents.

#### **DISCUSSION**

It is necessary to differentiate two subevent corner frequencies in our analysis from the double corner-frequency model (Archuleta and Ji, 2016; Denolle and Shearer, 2016; Uchide

**Figure 10.** (a) The normalized source time function and (b) slip distribution in Ye *et al.* (2016) for the 18 April 2014  $M_{\rm w}$  7.3 Guerrero earthquake. The black curve in panel (a) is the STF from finite-fault inversion and the red curve is its decomposition into two Brune sources. The white dashed circle in panel (b) with a radius  $r_{\rm FNT}=24$  km signifies the rupture area of the largest subevent. The best-fit Brune corner frequency is  $f_{\rm STF}=0.04$  Hz. (c) Radius  $r_{\rm STF}$  converting from  $f_{\rm STF}$  using k=0.32 as a function of the largest subevent radius  $r_{\rm FNT}$  measured from finite-fault inversion. The gray dashed line signifies a 1:1 relation. (d) Same as panel (c), but with k=0.23. The color version of this figure is available only in the electronic edition.

and Imanishi, 2016; Wang and Day, 2017). The double corner-frequency model has an additional corner compared to the Brune source model and variable fall-off rates, so it can better model complex source spectra at high frequency. The underlying physics of an additional corner is an extra time scale relating to one of the following source properties: the slip rise time (Brune, 1970), the time between the starting and stopping phases (Luco, 1985), the spacing of barriers and asperities (Denolle and Shearer, 2016), and the superposition of two subevents (Atkinson, 1993). Ji and Archuleta (2021) has systematically proposed two empirical double corner-frequency models that reproduce the mean peak ground acceleration,



the mean peak ground velocity, and the breakdown of self-similarity around magnitude  $M_{\rm w}$  5.3 using a stochastic ground motion model. Recently, Ji and Archuleta (2022) further showed that their models can be explained by fault geometry scaling relations and the high-frequency radiation is related to the fault plane aspect ratio. In comparison, our analysis assumes that each subevent is a Brune source model, and the complete earthquake is a superposition of several Brune sources. Most studies estimated a single corner frequency from the spectra of complete earthquakes, and our study aims to understand the best interpretation of these corner frequencies. Our model and double-frequency models are based on different source models, but both try to characterize the corner frequency that is critical for stress drop and ground-motion predictions. Our results also indicate that measuring stress drops of subevents can be important for constraining stress

**Figure 11.** (a) Spectra of the master event (black solid) with  $f_M=0.1\,$  Hz,  $M_M=5\,$  and the eGf (gray solid) with  $f_E=0.5\,$  Hz,  $M_E=0.5\,$  Hz as well as their spectral ratio (dashed line). (b)  $f_M$  as a function of  $f_E$  for  $T=+2\,$  s (blue) and  $T=-2\,$  s (red). The horizontal and vertical black dashed lines indicate the corner frequency  $f_M=0.19\,$  Hz of the master event. (c) Spectral ratios for  $T=+2\,$  s (blue) and  $T=-2\,$  s (red) when  $f_E=0.5\,$  Hz. The master event has the same spectra as the spectra shown in Figure 2. The corners  $f_M$  of the spectral ratio  $\Omega_M$  are indicated by reversed triangles for the cases where the large subevent precedes (in red) or succeeds (in blue) the small subevent by 2 s. (d) Same as panel (a) for  $f_E=1.5\,$  Hz. The color version of this figure is available only in the electronic edition.

drop for ground-motion simulations. Courboulex *et al.* (2022) found that the stress drop estimated from the total duration of the SCARDEC STF can be applied to ground-motion prediction for subduction zone earthquakes, implying

that using multiple subevents to constrain stress drops may significantly improve simulation performance.

Our decomposition approach is the same as Danré et al. (2019), but we assume the Brune source instead of the Gaussian source used in their analysis. The Gaussian source model is described by three source parameters and is thus more adaptable than the Brune source model with two parameters. Though Danré et al. (2019) resolved more subevents than found in this study, the relative number of subevents per faulting type are consistent in two studies, indicating that source models have little effect on the analysis. We also plot the subevent moment as a function of the earthquake moment (Fig. S1, available in the supplemental material to this article) and observe a positive correlation pattern, in agreement with their result. Furthermore, our finding that larger subevents tend to precede smaller subevents supports the conclusion in Danré et al. (2019) that the main event magnitude can be estimated after observing only the first few subevents, which can have significant impact on earthquake early warning. Both Danré et al. (2019) and our study showed that the smallest earthquakes have the fewest subevents, but both studies are limited by the decomposition method and the resolvable frequency bandwidth of SCARDEC STFs, which are obtained from teleseismic body-wave phases. Because teleseismic waveforms above 0.5 Hz have relatively low signal-to-noise ratios and STFs are averaged over stations, high-frequency contents are deficient in SCARDEC STFs. In addition, the decomposition method requires subevents to have moments that are at least 10% of the total moment. Therefore, it is likely that smaller subevents were missed by our analysis. The spectral analysis of regional and local seismograms would enable a study of the relationships of corner frequencies and rupture dimensions of subevents of  $M_{\rm w}$  3–4 earthquakes to test whether small earthquakes are as complex as large earthquakes (e.g., Fischer, 2005; Abercrombie, 2014; Ruhl et al., 2017).

SCARDEC STFs above 0.5 Hz are inaccurate due to the wave attenuation and wave propagation complexities as well as averaging of spectra from global stations. This inherent lack of high frequency of SCARDEC STFs reduces our resolution of subevents for smaller earthquakes. Figure S1 shows that the moment magnitude of the smallest subevent is constantly 1.3 smaller than the earthquake magnitude, which is also observed in Danré et al. (2019). The reason could either be that it is the smallest resolvable subevent magnitude due to limited frequency bandwidth or that it is truly the smallest subevent magnitude. Considering the available frequency bandwidth of SCARDEC STFs, subevents larger than  $M_{\rm w}$  5.5 should be resolvable, suggesting that at least the decomposition of earthquakes larger than  $M_{\rm w}$  6.9 should be accurate. In other words, earthquakes smaller than  $M_{\rm w}$  6.9 could be found to have more subevents given a higher frequency range.

One thing to be noted is that our analysis is from the teleseismic perspective. The results might be different from the regional perspective, because high-frequency energy of small subevents would be less attenuated and contribute more to the earthquake spectra. Stress-drop estimates of the same event using teleseismic and regional data have also been found to be disparate (e.g., Hartzell *et al.*, 2013). Therefore, additional tests using regional data are worth doing in the future, which, however, is out of the scope of this article.

# **CONCLUSIONS**

We use SCARDEC source time functions to investigate how estimates of the corner frequency of earthquakes with multiple subevents are biased by assuming a simple Brune source. By decomposing SCARDEC STFs using the Brune source model, we find more than half of  $M_{\rm w}$  5.5–8.0 earthquakes have multiple subevents. We derive theoretical solutions of the source spectrum for an earthquake with two Brune-type subevents. The theoretical derivation demonstrates that the earthquake corner frequency correlates better with the corner frequency of the large subevent than the small subevent. In both synthetic tests and the analysis of the SCARDEC catalog, earthquake corner frequency approaches the largest subevent corner frequency as the moment ratio between subevents increases, whereas the onset time difference between subevents has a minor effect with slight asymmetry. The positive correlation is also observed for earthquake rupture dimension estimated from its corner frequency and rupture dimension of the largest subevent estimated from finite-fault inversion. Our findings suggest that for the Brune source model, the corner frequency estimates may reflect the stress change of the largest asperity instead of the average stress drop on the whole rupture area, which helps to explain the commonly observed large variance of stress-drop estimates.

# **DATA AND RESOURCES**

All data and programming codes are archived in the Deep Blue Data repository at the website (doi: 10.7302/4ga6-8574). The supplemental material includes one figure. Source time functions used in this study were collected from the seismic source characteristic retrieved from deconvolving teleseismic body waves (SCARDEC) catalog at: http://scardec.projects.sismo.ipgp.fr/ (last accessed January 2022).

#### **DECLARATION OF COMPETING INTERESTS**

The authors acknowledge that there are no conflicts of interest recorded.

#### **ACKNOWLEDGMENTS**

This study is sponsored by the National Science Foundation award EAR-2019379. The authors thank Martin Vallée for advice on the source time functions in the SCARDEC catalog. The authors thank Associate Editor Adrien Oth and two anonymous reviewers for their constructive comments.

#### REFERENCES

- Abercrombie, R. E. (1995). Earthquake source scaling relationships from—1 to 5 ML using seismograms recorded at 2.5-km depth, *J. Geophys. Res.* **100**, no. B12, 24,015–24,036.
- Abercrombie, R. E. (2014). Stress drops of repeating earthquakes on the San Andreas fault at Parkfield, *Geophys. Res. Lett.* 41, no. 24, 8784–8791.
- Abercrombie, R. E. (2015). Investigating uncertainties in empirical Green's function analysis of earthquake source parameters, *J. Geophys. Res.* **120**, no. 6, 4263–4277.
- Abercrombie, R. E., X. Chen, and J. Zhang (2020). Repeating earthquakes with remarkably repeatable ruptures on the San Andreas fault at Parkfield, *Geophys. Res. Lett.* 47, no. 23, doi: 10.1029/2020GL089820.
- Allmann, B. P., and P. M. Shearer (2009). Global variations of stress drop for moderate to large earthquakes, *J. Geophys. Res.* **114,** no. B1, doi: 10.1029/2008JB005821.
- Allmann, B. P., and P. M. Shearer (2007). Spatial and temporal stress drop variations in small earthquakes near Parkfield, California, *J. Geophys. Res.* **112**, no. B4, doi: 10.1029/2006JB004395.
- Ando, R., and Y. Kaneko (2018). Dynamic rupture simulation reproduces spontaneous multifault rupture and arrest during the 2016 Mw 7.9 Kaikoura earthquake, *Geophys. Res. Lett.* **45**, no. 23, 12–875.
- Archuleta, R. J., and C. Ji (2016). Moment rate scaling for earthquakes  $3.3 \le M \le 5.3$  with implications for stress drop, *Geophys. Res. Lett.* **43**, no. 23, 12–004.
- Atkinson, G. M. (1993). Earthquake source spectra in eastern North America. *Bull. Seismol. Soc. Am.* **83**, no. 6, 1778–1798.
- Baltay, A., S. Ide, G. Prieto, and G. Beroza (2011). Variability in earth-quake stress drop and apparent stress, *Geophys. Res. Lett.* **38**, no. 6, doi: 10.1029/2011GL046698.
- Beresney, I., and G. Atkinson (2001). Subevent structure of large earthquakes—A ground-motion perspective, *Geophys. Res. Lett.* **28**, no. 1, 53–56.
- Boatwright, J. (1984). The effect of rupture complexity on estimates of source size, *J. Geophys. Res.* **89**, no. B2, 1132–1146.
- Branch, M. A., T. F. Coleman, and Y. Li (1999). A subspace, interior, and conjugate gradient method for large-scale bound-constrained minimization problems, *SIAM J. Sci. Comput.* **21,** no. 1, 1–23.
- Brune, J. N. (1970). Tectonic stress and the spectra of seismic shear waves from earthquakes, *J. Geophys. Res.* **100**, no. 26, 4997–5009.
- Chen, X., and P. M. Shearer (2011). Comprehensive analysis of earth-quake source spectra and swarms in the Salton trough, California, *J. Geophys. Res.* **116**, no. B9, doi: 10.1029/2011JB008263.
- Chounet, A., and M. Vallée (2018). Global and interregion characterization of subduction interface earthquakes derived from source time functions properties, *J. Geophys. Res.* **123**, no. 7, 5831–5852.
- Chounet, A., M. Vallée, M. Causse, and F. Courboulex (2018). Global catalog of earthquake rupture velocities shows anticorrelation between stress drop and rupture velocity, *Tectonophysics* 733, 148–158.
- Cooley, J. W., and J. W. Tukey (1965). An algorithm for the machine calculation of complex Fourier series, *Math. Comput.* **19**, no. 90, 297–301.
- Cotton, F., R. Archuleta, and M. Causse (2013). What is sigma of the stress drop? *Seismol. Res. Lett.* **84**, no. 1, 42–48.
- Courboulex, F., D. A. Castro-Cruz, A. Laurendeau, L. F. Bonilla, A. Alvarado, and E. Bertrand (2022). Ground motion simulations in Quito (Ecuador) due to major earthquakes from the subduction zone, *Geophys. J. Int.* 229, no. 3, 2192–2208.

- Courboulex, F., M. Vallée, M. Causse, and A. Chounet (2016). Stressdrop variability of shallow earthquakes extracted from a global database of source time functions, Seismol. Res. Lett. 87, no. 4, 912–918.
- Danré, P., J. Yin, B. P. Lipovsky, and M. A. Denolle (2019). Earthquakes within earthquakes: Patterns in rupture complexity, *Geophys. Res. Lett.* **46**, no. 13, 7352–7360.
- Das, S., and K. Aki (1977). Fault plane with barriers: A versatile earthquake model, *J. Geophys. Res.* **82**, no. 36, 5658–5670.
- Denolle, M. A. (2019). Energetic onset of earthquakes, *Geophys. Res. Lett.* **46**, no. 5, 2458–2466.
- Denolle, M. A., and P. M. Shearer (2016). New perspectives on self-similarity for shallow thrust earthquakes, *J. Geophys. Res.* **121**, no. 9, 6533–6565.
- Dziewonski, A. M., and D. L. Anderson (1981). Preliminary reference Earth model, *Phys. Earth Planet. In.* **25**, no. 4, 297–356.
- Fischer, T. (2005). Modelling of multiple events using empirical Green's functions: Method, application to swarm earthquakes and implications for their rupture propagation, *Geophys. J. Int.* **163**, no. 3, 991–1005.
- Gallovič, F., and L. Valentová (2020). Earthquake stress drops from dynamic rupture simulations constrained by observed ground motions, *Geophys. Res. Lett.* 47, no. 4, doi: 10.1029/2019GL085880.
- García, D., S. K. Singh, M. Herráiz, J. F. Pacheco, and M. Ordaz (2004). Inslab earthquakes of central Mexico: Q, source spectra, and stress drop, *Bull. Seismol. Soc. Am.* 94, no. 3, 789–802.
- Hayes, G. P. (2017). The finite, kinematic rupture properties of great-sized earthquakes since 1990, *Earth Planet. Sci. Lett.* **468**, 94–100.
- Hartzell, S., C. Mendoza, and Y. Zeng (2013). Rupture model of the 2011 Mineral, Virginia, earthquake from teleseismic and regional waveforms, *Geophys. Res. Lett.* 40, no 21, 5665–5670.
- Huang, Y., and J. P. Ampuero (2011). Pulse-like ruptures induced by low-velocity fault zones, *J. Geophys. Res.* **116**, no. B12, doi: 10.1029/2011JB008684.
- Huang, Y., G. C. Beroza, and W. L. Ellsworth (2016). Stress drop estimates of potentially induced earthquakes in the Guy-Greenbrier sequence, *J. Geophys. Res.* **121**, no. 9, 6597–6607.
- Ji, C., and R. J. Archuleta (2021). Two empirical double-corner-frequency source spectra and their physical implications, *Bull. Seismol. Soc. Am.* 111, no. 2, 737–761.
- Ji, C., and R. J. Archuleta (2022). A source physics interpretation of nonself-similar double-corner-frequency source spectral model JA19\_2S, Seismol. Res. Lett. 93, no. 2A, 777–786.
- Kaneko, Y., and P. M. Shearer (2015). Variability of seismic source spectra, estimated stress drop, and radiated energy, derived from cohesive-zone models of symmetrical and asymmetrical circular and elliptical ruptures, *J. Geophys. Res.* **120**, no. 2, 1053–1079.
- Kaneko, Y., and P. M. Shearer (2014). Seismic source spectra and estimated stress drop derived from cohesive-zone models of circular subshear rupture, *Geophys. J. Int.* 197, no. 2, 1002–1015.
- Lay, T., and H. Kanamori (1981). An asperity model of large earth-quake sequences, *Earthquake Prediction* **4**, 579–592, doi: 10.1029/ME004p0579.
- Lay, T., H. Kanamori, and L. Ruff (1982). The asperity model and the nature of large subduction zone earthquakes, *Earthq. Predict. Res.* 1, no. 1, 3–71.
- Li, Y., C. Doll Jr, and M. N. Toksöz (1995). Source characterization and fault plane determination for MbLg= 1.2 to 4.4 earthquakes in

- the Charlevoix seismic zone, Quebec, Canada, *Bull. Seismol. Soc. Am.* **85**, no. 6, 1604–1621.
- Lin, Y. Y., and N. Lapusta (2018). Microseismicity simulated on asperity-like fault patches: On scaling of seismic moment with duration and seismological estimates of stress drops, *Geophys. Res. Lett.* **45**, no. 16, 8145–8155.
- Liu, M., Y. Huang, and J. Ritsema (2020). Stress drop variation of deep-focus earthquakes based on empirical green's functions, *Geophys. Res. Lett.* 47, no. 9, doi: 10.1029/2019GL086055.
- Luco, J. E. (1985). On strong ground motion estimates based on models of the radiated spectrum, Bull. Seismol. Soc. Am. 75, no. 3, 641–649.
- Madariaga, R. (1976). Dynamics of an expanding circular fault, *Bull. Seismol. Soc. Am.* **66**, no. 3, 639–666.
- Noda, H., N. Lapusta, and H. Kanamori (2013). Comparison of average stress drop measures for ruptures with heterogeneous stress change and implications for earthquake physics, *Geophys. J. Int.* **193**, no. 3, 1691–1712.
- Oth, A. (2013). On the characteristics of earthquake stress release variations in Japan, *Earth Planet. Sci. Lett.* **377**, 132–141.
- Papageorgiou, A. S., and K. Aki (1983). A specific barrier model for the quantitative description of inhomogeneous faulting and the prediction of strong ground motion. I. Description of the model, *Bull. Seismol. Soc. Am.* 73, no. 3, 693–722.
- Prieto, G. A., B. Froment, C. Yu, P. Poli, and R. Abercrombie (2017).
  Earthquake rupture below the brittle-ductile transition in continental lithospheric mantle, Sci. Adv. 3, no. 3, doi: 10.1126/sciadv.1602642.
- Purvance, M. D., and J. G. Anderson (2003). A comprehensive study of the observed spectral decay in strong-motion accelerations recorded in Guerrero, Mexico, *Bull. Seismol. Soc. Am.* 93, no. 2, 600–611.
- Ruhl, C. J., R. E. Abercrombie, and K. D. Smith (2017). Spatiotemporal variation of stress drop during the 2008 Mogul, Nevada, earthquake swarm, *J. Geophys. Res.* **122**, no. 10, 8163–8180.
- Sato, T., and T. Hirasawa (1973). Body wave spectra from propagating shear cracks, *J. Phys. Earth* **21**, no. 4, 415–431.
- Shearer, P. M., R. E. Abercrombie, D. T. Trugman, and W. Wang (2019). Comparing EGF methods for estimating corner frequency and stress drop from P wave spectra, J. Geophys. Res. 124, no. 4, 3966–3986.
- Shearer, P. M., G. A. Prieto, and E. Hauksson (2006). Comprehensive analysis of earthquake source spectra in southern California, *J. Geophys. Res.* **111**, no. B6, doi: 10.1029/2005JB003979.
- Sotiriadis, D., B. Margaris, N. Klimis, and A. Sextos (2021). Implications of high-frequency decay parameter, "κ-kappa", in

- the estimation of kinematic soil-structure interaction effects, Soil Dynam. Earthq. Eng. 144, 106,665.
- Trugman, D. T., S. L. Dougherty, E. S. Cochran, and P. M. Shearer (2017). Source spectral properties of small to moderate earth-quakes in southern Kansas, *J. Geophys. Res.* **122**, no. 10, 8021–8034.
- Uchide, T., and K. Imanishi (2016). Small earthquakes deviate from the omega-square model as revealed by multiple spectral ratio analysis, *Bull. Seismol. Soc. Am.* **106**, no. 3, 1357–1363.
- Ulrich, T., A. A. Gabriel, J. P. Ampuero, and W. Xu (2019). Dynamic viability of the 2016 Mw 7.8 Kaikōura earthquake cascade on weak crustal faults, *Nat. Comm.* **10**, no. 1, 1–16.
- Vallée, M. (2013). Source time function properties indicate a strain drop independent of earthquake depth and magnitude, *Nat. Comm.* **4,** no. 1, 1–6.
- Vallée, M., and V. Douet (2016). A new database of source time functions (STFs) extracted from the SCARDEC method, *Phys. Earth Planet. In.* **257**, 149–157.
- Wang, Y., and S. M. Day (2017). Seismic source spectral properties of crack-like and pulse-like modes of dynamic rupture, *J. Geophys. Res.* **122,** no. 8, 6657–6684.
- Wang, E., A. M. Rubin, and J. P. Ampuero (2014). Compound earth-quakes on a bimaterial interface and implications for rupture mechanics, *Geophys. J. Int.* 197, no. 2, 1138–1153.
- Wu, Q., M. Chapman, and X. Chen (2018). Stress-drop variations of induced earthquakes in Oklahoma, *Bull. Seismol. Soc. Am.* 108, no. 3A, 1107–1123.
- Ye, L., T. Lay, H. Kanamori, and L. Rivera (2016). Rupture characteristics of major and great (Mw≥ 7.0) megathrust earthquakes from 1990 to 2015: 1. Source parameter scaling relationships, *J. Geophys. Res.* **121**, no. 2, 826–844.
- Yin, J., Z. Li, and M. A. Denolle (2021). Source time function clustering reveals patterns in earthquake dynamics, *Seismol. Res. Lett.* 92, no. 4, 2343–2353.
- Yu, H., R. M. Harrington, H. Kao, Y. Liu, R. E. Abercrombie, and B. Wang (2020). Well proximity governing stress drop variation and seismic attenuation associated with hydraulic fracturing induced earthquakes, J. Geophys. Res. 125, no. 9, doi: 10.1029/2020JB020103.

Manuscript received 29 September 2022 Published online 4 January 2023